Anisotropy-induced depinning in the Zn-substituted skyrmion host Cu_2OSeO_3

M. T. Birch,[1,2] S. H. Moody,[1] M. N. Wilson,[1] M. Crisanti,[3,4] O. Bewley,[1] A. Štefančič,[3,*] G. Balakrishnan,[3] R. Fan,[2] P. Steadman,[2] D. Alba Venero,[5] R. Cubitt,[4] and P. D. Hatton[1]

[1]*Durham University, Centre for Materials Physics, Durham DH1 3LE, United Kingdom*
[2]*Diamond Light Source, Didcot OX11 0DE, United Kingdom*
[3]*Department of Physics, University of Warwick, Coventry CV4 7AL, United Kingdom*
[4]*Institut Laue-Langevin, CS 20156, 38042 Grenoble Cedex 9, France*
[5]*ISIS Neutron and Muon Source, Rutherford Appleton Laboratory, Didcot OX11 0QX, United Kingdom*

(Received 20 June 2020; accepted 2 September 2020; published 18 September 2020)

Magnetic skyrmions are nanosized topological spin textures stabilized by a delicate balance of magnetic energy terms. The chemical substitution of the underlying crystal structure of skyrmion-hosting materials offers a route to manipulate these energy contributions but also introduces additional effects such as disorder and pinning. While the effects of doping and disorder have been well studied in B20 metallic materials such as $Fe_{1-x}Co_xSi$ and $Mn_{1-x}Fe_xSi$, the consequences of chemical substitution in the magnetoelectric insulator Cu_2OSeO_3 have not been fully explored. In this work we utilize a combination of AC magnetometry and small-angle neutron scattering to investigate the magnetic phase transition dynamics in pristine and Zn-substituted Cu_2OSeO_3. The results demonstrate that the first-order helical-conical phase transition exhibits two thermally separated behavioral regimes: at high temperatures, the helical and conical domains transform by large-scale, continuous rotations, while at low temperatures, the two phases coexist. Remarkably, the effects of pinning in the substituted sample are less prevalent at low temperatures compared to high temperatures, despite the reduction of available thermal activation energy. We attribute this behavior to the large, temperature-dependent, cubic anisotropy unique to Cu_2OSeO_3, which becomes strong enough to overcome the pinning energy at low temperatures. Consideration and further exploration of these effects will be crucial when engineering skyrmion materials towards future applications.

DOI: 10.1103/PhysRevB.102.104424

I. INTRODUCTION

Magnetic skyrmions are nanoscale, topologically protected particles [1]. In conductive samples, it has been shown that under the application of a current they have high mobility [2]. These properties have made skyrmions the focus of recent research due to their potential application in future spintronic devices [3]. The presence of the Dzyaloshinskii-Moriya interaction (DMI) is vital for the formation magnetic skyrmions in a range of material systems [4]. Interfacial DMI, induced by spin-orbit coupling at the interface between layers in thin films, produces Néel-type skyrmions [5–7]. In chiral magnets, such as MnSi [8,9], MnGe [10], $Fe_{1-x}Co_xi$ [11,12], FeGe [13,14], the multiferroic Cu_2OSeO_3 [15] and the β-Mn type Co-Zn-Mn alloys [16], the lack of centrosymmetry in the underlying atomic lattice gives rise to bulk DMI, leading to the formation of Bloch-type skyrmions, or in the case of the polar materials GaV_4Se_8 and GaV_4S_8, Néel-type skyrmions [17–19].

In these bulk materials, the interplay of the DMI with the exchange and dipolar interactions, the Zeeman energy, and the magnetocrystalline anisotropies are responsible for a range of magnetic structures and phenomena [3]. At zero applied magnetic field the helical state is realized by the competition of the exchange and DMI [20]. Typically, multiple degenerate helical domains order and orient to point their spins along easy planes, as determined by the underlying cubic anisotropy. Under an applied magnetic field, the Zeeman energy lifts the helical domain degeneracy, reorienting the magnetic structures such that their spin propagation vectors point along the field direction, forming the conical state. Close to the Curie temperature T_c, critical thermal fluctuations are responsible for stabilizing the hexagonal skyrmion lattice against the conical state in a small range of applied magnetic field [3]. However, it has been demonstrated that by cooling the system under an applied magnetic field, skyrmions may survive in a metastable state beyond the typical equilibrium range [21–27].

The role of cubic anisotropy has been highlighted in a number of recent studies. By utilizing the wide temperature and applied field range of the metastable skyrmion state a transition from the typical hexagonal arrangement to a square skyrmion lattice has been observed in both MnSi [28] and $Co_8Zn_8Mn_4$ [21], induced by the increased effective anisotropy strength at low temperatures. Recently, a rhombiclike distortion of the hexagonal skyrmion lattice has been reported in $Co_{10}Zn_{10}$, also as a result of the magnetocrystalline anisotropy [23]. Meanwhile, in Cu_2OSeO_3 the

*Present address: Electrochemistry Laboratory, Paul Scherrer Institut, CH-5232 Villigen PSI, Switzerland.

strong spin-orbit coupling results in a comparatively large, temperature-dependent cubic anisotropy in comparison to $Fe_{1-x}Co_xSi$ and MnSi, as illustrated in previous work [29]. For example, the anisotropy constant in Cu_2OSeO_3 has been estimated to be $K = \sim 400$ J/m^3 [30], compared to a value of $K = \sim -120$ J/m^3 in FeGe [31]. At low temperatures, the anisotropy in Cu_2OSeO_3 is of sufficient strength to rotate the conical state away from the applied magnetic field direction, forming the tilted conical state [32], and is further responsible for the stabilization of the equilibrium low-temperature skyrmion state over much of the temperature-field phase diagram [30,33]. These discoveries highlight the rich variety of spin textures accessible by manipulating the balance of interaction energies in chiral magnets.

One way to control the relative contribution of these energy terms is by varying the elemental composition of skyrmion-hosting materials via chemical substitution or doping. Compositional effects have been studied in a range of systems, such as $Fe_{1-x}Co_xSi$ [34–36], $Mn_{1-x}(Fe/Co)_xSi$ [37–40], $Mn_{1-x}Fe_xGe$ [41–44], $MnSi_{1-x}Ge_x$ [45], $Co_{10-x}Zn_{10-y}Mn_{x+y}$ [16,22,23,46], $Co_{8-x}(Fe/Ni/Ru)_xZn_8Mn_4$ [47], $GaV_4(S_{8-x}Se_x)$ [48,49], $[Cu_{1-x}(Zn/Ni)_x]_2OSeO_3$ [50–55], and $Cu_2OSe_{1-x}Te_xO_3$ [56]. The properties altered include variation of T_c, indicating a change in the exchange interaction strength; alteration of the magnitude and sign of the DMI, leading to changes in the helical and skyrmion lattice periodicity and chirality; switching of the magnetic easy axes, and therefore the helical ground-state domain orientation, by tuning of the cubic anisotropy constants; and modification of the spin wave propagation.

Furthermore, it was demonstrated that the disorder present in the underlying atomic lattice of these doped systems introduced pinning effects which allowed the formation of larger populations of metastable skyrmions when field cooling at lower cooling rates [11] and increased both the annihilation and formation time of the skyrmion state [53,54]. This pinning can affect other dynamic behaviors such as current-induced skyrmion motion—a phenomenon crucial to proposed skyrmion racetrack devices [57,58]. Extrinsic defects and impurities can attract or repel skyrmions [59], or act as nucleation or annihilation sites [60], which might be exploited for technological implementation. In combination with alterations to the energy balance mentioned above, these dynamical pinning effects must be considered when engineering the properties of skyrmion materials for future applications.

In this work we utilize detailed AC magnetometry and small-angle neutron scattering (SANS) to investigate the effect of doping, and the role of cubic anisotropy, in helimagnetic phase transitions in $(Cu_{1-x}Zn_x)_2OSeO_3$. Beginning with an explanation of the experimental methods in Sec. II, we proceed to detail the spin textures exhibited by Cu_2OSeO_3 in Sec. III. Typical phase diagrams are considered in Sec. IV, revealing the AC susceptibility signals exhibited by each magnetic state. This is followed by Sec. V, where the detailed features of the real and imaginary components of the AC susceptibility measurements are examined and interpreted. Comparison of the helical-conical phase boundary in both samples reveals significant history-dependent pinning behavior in the substituted sample. Further investigation of the dissipative effects indicated by peaks in the imaginary component reveals unexpected low-temperature behavior in both samples.

The results of the SANS measurements are considered in Sec. VI, with reference to the associated features of the AC susceptibility data in Sec. V. The volume fractions of all magnetic structures are assessed, revealing that the helical-conical phase transition exhibits two distinct, thermally separated behavioral regimes. In Sec. VII we examine temperature-dependent SANS measurements and, with comparison to previous studies of other chemically substituted skyrmion materials, discuss the observed behavior in the context of the large, temperature-dependent cubic anisotropy exhibited by Cu_2OSeO_3, which may explain the behavior observed in this study. Finally, we summarize the results and conclusions in Sec. VIII.

II. METHODS

Single crystals of Cu_2OSeO_3 were grown from polycrystalline powders using the chemical vapor transport method [52]. The elemental composition of the resulting crystals was determined by inductively coupled plasma mass spectroscopy, as reported in previous work [52]. The samples chosen for this study were a pristine Cu_2OSeO_3 crystal, with $x = 0.00$, or 0% Zn substitution, and a $(Cu_{1-x}Zn_x)_2OSeO_3$ crystal with $x = 0.02$, or 2% Zn substitution.

Magnetometry measurements were performed with a superconducting quantum interference device magnetometer (MPMS3, Quantum Design) fitted with the AC magnetometry option. Temperature control was achieved by utilizing the built-in helium cryostat. The samples were attached to a quartz rod using GE varnish and mounted in the system with the [110] crystal direction parallel to the applied magnetic field. Measurements of magnetization vs temperature determined the T_C of the 0% and 2% samples to be 58.8 and 57.3 K, respectively. AC susceptibility measurements were performed with an oscillating magnetic field amplitude of 0.1 mT at a frequency of 10 Hz, and all cooling procedures were performed at a rate of 40 K/min.

SANS measurements were performed on the D33 instrument at the Institut Laue-Langevin (ILL) reactor (Figs. 5–10) and the ZOOM instrument [61] at the ISIS spallation source (Fig. 11). The samples were attached to a 200-μm-thick aluminum plate and placed inside a helium cryostat equipped with superconducting magnets. At ILL a neutron wavelength of 6.0 Å was selected with a FWHM spread of $\lambda/\lambda = 10\%$. Due to ISIS being a time-of-flight source, a range of neutron wavelengths were accepted between 1.75 and 17.5 Å. Cooling procedures were performed at a rate of 7 and 0.5 K/min at ILL and ISIS, respectively. A schematic of the experimental setup is shown in Fig. 1(a). During diffraction measurements, coherent scattering is observed when the orientation of the magnetic structures fulfill the Bragg condition. For SANS, this occurs when the direction of periodicity of the magnetic structure is close to perpendicular to the incident neutron beam, resulting in detection of a diffraction peak, or magnetic satellite.

Each Cu_2OSeO_3 crystal was positioned with the [110] axis parallel to the applied magnetic field and the $[1\bar{1}0]$ direction aligned with the vertical rotation axis, as shown in Fig. 1. A

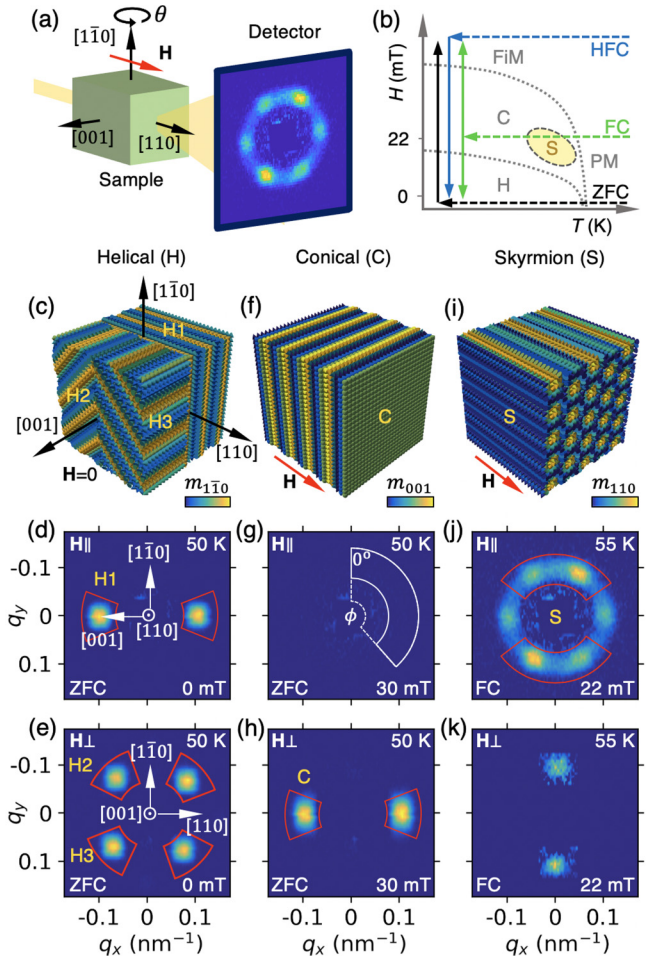

FIG. 1. (a) Schematic illustration of the small-angle neutron-scattering experiment setup. The sample and applied field can be rotated together through θ to measure with the magnetic field directed both parallel and perpendicular to the neutron beam. The relative orientation of the Cu_2OSeO_3 sample is shown. (b) An example skyrmion material phase diagram showing the helical (H), conical (C), skyrmion (S), ferrimagnetic (FiM), and paramagnetic (PM) states. Representations of the zero-field-cooled (ZFC), high-field-cooled (HFC), and field-cooled (FC) procedures are shown. Three-dimensional visualizations of the spin textures and characteristic SANS patterns measured for the helical (c–e), conical (f–h), and skyrmion states (i–k) states, with the field both parallel (d, g, j) and perpendicular (e, h, k) to the neutron beam. Sector boxes indicate regions of scattering summed to report intensities in subsequent figures. The azimuthal angle around each SANS pattern, ϕ, is illustrated in panel (g).

rotation around this axis through θ rotates both the sample and applied magnetic field simultaneously. All SANS patterns shown are the result of summing scans measured as a function of this rocking angle θ. In this particular sample and field setup, scattering peaks from all ordered chiral magnetic structures exhibited by the sample may be observed by rotating the sample and field through 90 degrees such that the applied field is positioned either parallel or perpendicular to the neutron beam. For the rest of the article, these two sample orientations will be referred to as the "field-parallel" and "field-perpendicular" configurations, respectively.

In this study we employed three distinct field-temperature protocols, as illustrated in Fig. 1(b). In the zero-field-cooled (ZFC), field-cooled (FC), and high-field-cooled (HFC) procedures, the sample was cooled to the target temperature under an applied magnetic field of 0, 20, and 200 mT, respectively. After initializing the magnetic state under these conditions, measurements were carried out as a function of increasing (ZFC) and decreasing (HFC) applied magnetic field. In the case of the FC procedure, measurements were performed for increasing and decreasing magnetic field after two separate cooling procedures. Metastable skyrmions were formed only during the FC protocol, as this field-temperature cooling path took the sample through the equilibrium skyrmion phase.

III. CHIRAL MAGNETIC STATES

Illustrations of the spin textures exhibited by Cu_2OSeO_3, and their corresponding SANS patterns in the two experimental configurations, are displayed in Fig. 1. At zero magnetic field the helical structure is the equilibrium state, consisting of a continuous rotation of spins orthogonal to a propagation vector. In Cu_2OSeO_3 this vector aligns along the ⟨100⟩ crystal axes due to the cubic anisotropy present in the system, giving rise to three distinct helical domains labeled H1, H2, and H3 in Fig. 1(c). Scattering from these domains can be observed in the field-parallel configuration (H1) or in the field-perpendicular configuration (adding the scattering from both H2 and H3 domains: H2,3), as shown in Figs. 1(d) and 1(e).

Upon increasing the applied magnetic field, the helical state degeneracy is lifted and the structure transforms to the conical state illustrated in Fig. 1(f), consisting of a continuous rotation of spins at an acute angle to the propagation vector which is aligned to the applied field. In the field-parallel configuration, no magnetic scattering is observed, as displayed in Fig. 1(g), while in the field-perpendicular orientation, a single pair of conical magnetic satellites are observed, labeled C in Fig. 1(h). At higher applied magnetic field, the angle of the spins to the propagation vector is reduced, resulting in a lower intensity of the magnetic diffraction peaks before a ferrimagnetic texture is reached.

Close to 55 K and 22 mT, the skyrmion state is formed in a plane perpendicular to the applied magnetic field, as illustrated in Fig. 1(i). This image highlights the elongated tubelike structure exhibited by magnetic skyrmions in bulk materials [26]. In the field-parallel configuration, six magnetic scattering peaks are observed, a characteristic signature of the hexagonal skyrmion lattice, labeled S in Fig. 1(j). Due to rotational disorder of the skyrmion lattice, weak scattering can be observed in the field-perpendicular configuration, as shown in Fig. 1(k). This corresponds to the intensity at the top of the ring of scattering in Fig. 1(j). For further analysis, in this study we report the intensities of the H1, H2, H3, C, and S magnetic peaks. These intensities were calculated by summing the total counts measured inside the red-sector boxes specified in Figs. 1(d)–1(k).

IV. AC SUSCEPTIBILITY PHASE DIAGRAMS

Magnetic phase diagrams are shown in Fig. 2 for the pristine and 2% Zn-substituted samples measured using AC

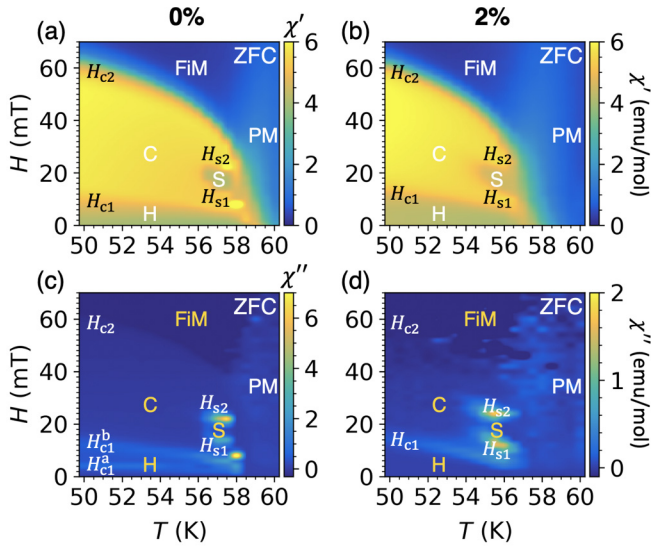

FIG. 2. (a–d) Magnetic phase diagrams, as determined by AC susceptibility measurements following the ZFC procedure, for the 0% and 2% Zn-substituted samples, respectively, highlighting the helical (H), conical (C), skyrmion (S), ferrimagnetic (FiM), and paramagnetic (PM) states. The real component χ' is plotted in (a, b) and the imaginary component χ'' in (c, d). Critical fields marking the phase boundaries between the H and C (H_{c1}, H_{c1}^a, H_{c1}^b), C and FiM (H_{c2}), and S and C ($H_{s1,2}$) states are labeled.

susceptibility magnetometry. In Figs. 2(a) and 2(b), the color map directly plots the real component of the AC susceptibility χ', measured as a function of applied magnetic field after ZFC to temperatures between 50 and 60 K. At the low-frequency limit, this quantity measures the local gradient of the magnetization with the applied field and is useful for distinguishing the temperature and field extent of the magnetic phases.

The boundaries between these magnetic phases are denoted by critical fields H_x. The helical state can be identified by the reduced value of χ' close to 0 mT and extending for an increasing field up to H_{c1} at the boundary with the conical state. In turn, the conical state exists up to H_{c2} before transitioning to the field-polarized state, characterized by a reduction in χ'. Close to T_C the skyrmion state can be identified by the characteristic dip in AC susceptibility at ∼20 mT, a well-established signature common to skyrmion-hosting bulk chiral magnets [13]. The lower and upper field boundaries of this phase are denoted H_{s1} and H_{s2}, respectively. Looking at this real component, the phase diagrams for both the pristine and substituted sample show no dramatic differences besides the reduction of T_C with increased Zn content.

At specific probe frequencies dynamic processes may be excited, causing a phase difference between the oscillating magnetization and the drive field. This manifests as a signal in the imaginary component of the AC susceptibility χ'', indicating relaxation-induced energy losses [62]. The dissipation is associated with thermodynamically irreversible dynamic processes such as domain wall motion or, at a phase boundary, excitation between two competing magnetic phases [63]. The χ'' component of the AC susceptibility for both samples is plotted in Figs. 2(c) and 2(d).

Second-order phase transitions, characterized by the continuous transformation of one state into another, are not expected to exhibit a χ'' signal. This can be seen by the lack of a χ'' peak at H_{c2} in both Figs. 2(c) and 2(d), as the conical state continuously deforms to the ferrimagnetic state. On the other hand, for first-order phase transitions, characterized by coexistence of the two phases in the vicinity of the transition, a χ'' signal can be expected: there is significant energy loss occurring as the oscillating magnetic field drives the boundaries between the two coexisting phase volumes [29]. Such an effect is observed at the edges of the equilibrium skyrmion phase in Figs. 2(c) and 2(d), H_{s1} and H_{s2}, where a large χ'' signal is exhibited, indicating the annihilation and formation of skyrmions to and from the conical state [34]. Further χ'' peaks seen at H_{c1} indicate the helical-to-conical first-order phase transition.

The magnitude of χ'' peaks associated with first-order magnetic phase transitions can be modified by several factors [63]. First, χ'' exhibits a frequency dependence, with the maximum indicating the characteristic frequency of the excited dynamic processes [36,64]. Therefore as we only measure at 10 Hz, a change in the size of the χ'' peaks could be associated with a shift of this characteristic frequency or a broadening of the resonance due to the introduction of a range of relaxation timescales [65]. Second, the peak can be reduced when phase coexistence in the first-order transition is suppressed, as there can be no excitation between the two magnetic states and therefore no energy losses [29]. Such an effect can be seen by the lack of χ'' signal at the low-temperature edge of the equilibrium skyrmion phase in Figs. 2(c) and 2(d), where less of the sample enters the skyrmion phase and where the associated dynamics are increasingly slow and metastable [64]. Finally, when considering the decay of a metastable state, transitions to the ground state are energetically preferred. Thus the oscillating field may only drive the transition in one direction and no dissipative signal is expected [29], despite the coexistence of the magnetic states.

V. TEMPERATURE-DEPENDENT AC SUSCEPTIBILITY DATA

In the following sections we shall explore the detailed features of AC susceptibility data at each temperature, as shown in Fig. 3, while discussing the implications of these behaviors with reference to the summary panels in Fig. 4. AC susceptibility data sets measured at a range of temperatures for both the pristine and substituted samples, and following the ZFC, HFC, and FC measurement procedures, are shown in Fig. 3. Critical field points at each phase boundary are indicated by the colored vertical lines and were determined by features in the data.

The H_{c2} points were estimated to be at the inflection point in the χ'' data at high fields, most easily seen in Fig. 3(a3). Below the equilibrium skyrmion phase, no obvious feature exists for the upper skyrmion phase boundaries H_{s2} and the majority of the lower boundaries H_{s1}. Therefore these values were estimated by comparing features in the χ' data following the FC and ZFC/HFC procedures. For all the H_{c1}, H_{c1}^a, and H_{c1}^b points, and for H_{s1} points below 40 K in the substituted

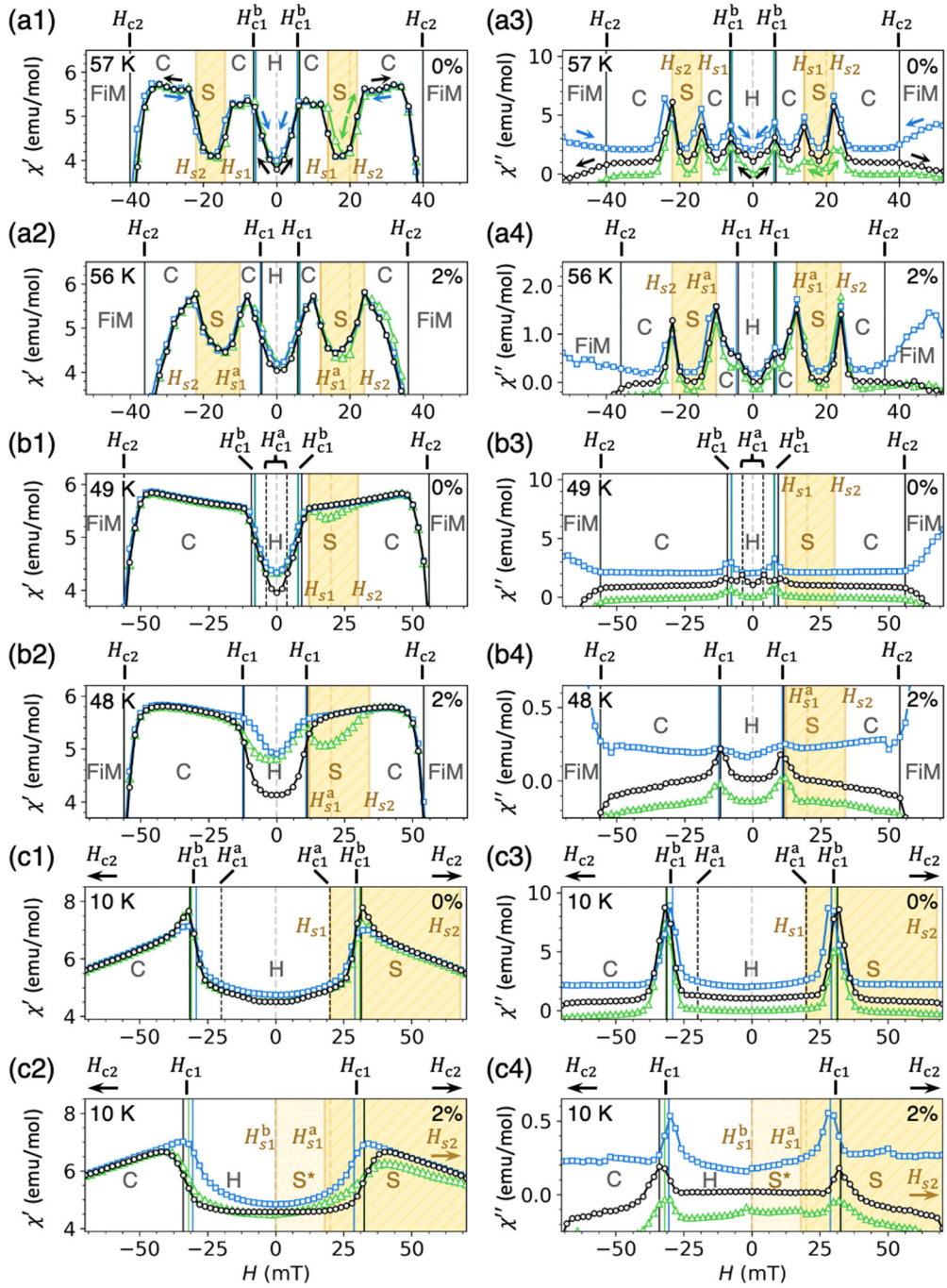

FIG. 3. (a)–(c) The real, χ' (1 and 2), and imaginary, χ'' (3 and 4), components of the AC susceptibility data measured as a function of magnetic field at selected temperatures for the pristine (1 and 3) and substituted (2 and 4) samples. Data acquired following the ZFC (black circles), HFC (blue squares), and FC (green triangles) measurement procedures is shown. The χ'' data has been vertically offset to allow the features to be inspected, adding or subtracting by the following amounts: 0% ZFC +1.0; 0% FC +2.0; 2% HFC +0.15; and 2% FC −0.15. Colored vertical lines indicate the fitted critical field values for each phase transition following each measurement procedure. The yellow filled regions indicate the extent of the skyrmion state after FC. The locations of the helical (H), conical (C), skyrmion (S, S*), and ferrimagnetic (FiM) states are labeled. The features at ∼50 mT in the HFC data in (b4) and (c4) appear to be temperature-independent instrumental effects.

sample, the field value was obtained by fitting a Gaussian peak with a linear background to the associated peak in the χ'' data.

A summary of the fitted/estimate values of the critical fields H_x following each measurement procedure is plotted as a function of temperature in Figs. 4(a) and 4(b), forming an extended magnetic phase diagram for the pristine and substituted samples. In Figs. 4(c) and 4(d), the fitted magnitudes of the χ'' peaks (taken as the area under each peak) at H_{c1} and H_{s1} are plotted as a function of temperature for each sample.

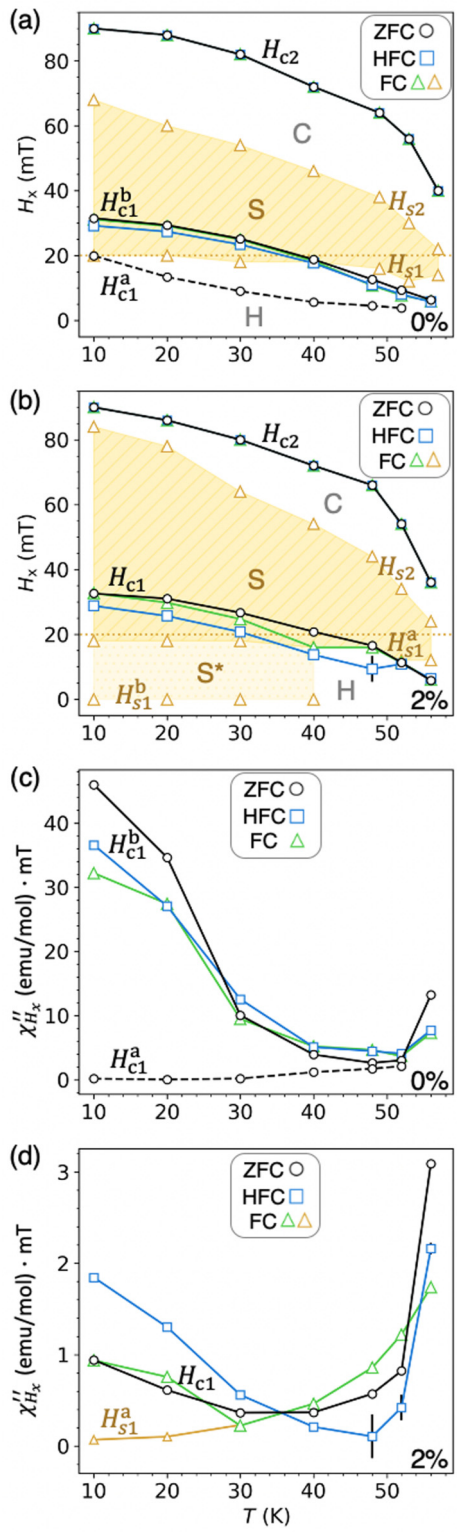

FIG. 4. (a, b) Low-temperature magnetic phase diagrams for the pristine and substituted samples, formed by plotting the critical field values determined for each measurement procedure vs temperature, as labeled. Filled yellow regions designate the existence of the skyrmion state after FC. The locations of the helical (H), conical (C), skyrmion (S, S*), and ferrimagnetic (FiM) states are labeled. (c, d) The fitted magnitude of the peak in the χ'' data for the H_{c1} and H_{s1} critical fields after each measurement procedure for the pristine and substituted samples, respectively.

A. Equilibrium skyrmion phase

We first consider the data in Fig. 3(a), recorded at 57 and 56 K for the pristine and substituted samples, respectively. At these temperatures the samples exhibit the equilibrium skyrmion phase, indicated by the yellow filled regions at positive and negative applied magnetic fields. The difference in the overall shape of the χ' data between the samples, shown in Figs. 3(a1) and 3(a2), can be attributed to the fact the measurements were not taken at the exact same temperature relative to T_C ($T_C - T = 1.8$ and 1.3 K for the pristine and substituted samples, respectively). For each sample at this high temperature, there are no obvious differences in the data between the ZFC, HFC, and FC measurement procedures: the fitted values of all critical fields are consistent with each other.

However, comparing Figs. 3(a3) and 3(a4), the magnitude of the χ'' peaks in the substituted sample is far smaller in comparison to the pristine sample. Such a compositional effect has been observed in $Mn_{1-x}Fe_xSi$, where the χ'' signal around the skyrmion phase was reduced for $x > 0.03$ [39], and it was argued that this indicated a decrease in the characteristic frequency of the transition due to a slowing down of the dynamics by pinning effects. Therefore, following the arguments in Sec. IV, the reduction of the χ'' signals in our substituted sample could either be caused by a broadening of the frequency dependence or the introduction of metastable effects due to the additional pinning dynamics. The SANS data explored in later sections sheds some light on this issue, but thoroughly distinguishing between these scenarios requires future measurement of frequency-dependent data.

B. Helical-conical phase transition

Next we shall consider the behavior of the helical-conical phase transition as a function of temperature. Turning first to the χ' data at 49 K in Fig. 3(b1), there is a difference in the measured value of χ' at around 0 mT following the ZFC and HFC procedures: the value of χ' it larger at 0 mT after HFC than it is after ZFC. This behavior indicates that when following the HFC procedure the conical-to-helical phase transition results in a helical state different to the one formed upon ZFC—perhaps with altered relative volumes of the H1 and H2,3 helical domains. This effect is more pronounced in the substituted sample, as can be seen in Fig. 3(b2), suggesting that the Zn substitution is hindering the conical-to-helical phase transition in some manner. However, for both samples this low field divergence between the HFC and ZFC data is reduced at the lower temperature of 10 K, as shown in Figs. 3(c1) and 3(c2). This is surprising, as one might expect the effects of pinning in the substituted sample to be more prevalent at lower temperatures, as there is less thermal energy available to enable depinning.

In the χ'' data we see that at temperatures lower than the equilibrium skyrmion pocket, only peaks associated with helical-conical phase transition are seen. In the pristine sample two peaks are seen, labeled H^a_{c1} and H^b_{c1}, respectively. In Cu_2OSeO_3 these two distinct peaks have previously been attributed to the distinct reorientation of H1 and H2,3 domains to the conical state when the field is applied along the [110] [33]. However, in the substituted sample, the H^a_{c1} peaks are not

observed, suggesting that pinning effects may suppress this behavior.

Unlike at high temperatures in Fig. 3(a), at 49 K and below we can see that there is a field offset in the peak position of the χ'' data when comparing each measurement procedure, indicating history-dependent behavior in the H_{c1} phase transition point. The fitted H_{c1} values for both samples are summarized in Figs. 4(a) and 4(b), respectively, highlighting that this hysteretic field offset becomes significant below 50 K and is more pronounced in the substituted sample.

At 49 and 48 K, it is evident that in both samples the magnitudes of the χ'' peaks are greatly reduced relative to the data measured at 57 and 56 K. However, remarkably, looking at the data in Figs. 3(c3) and 3(c4), we can see that the χ'' peaks are actually larger in size at the lower temperature 10 K. This temperature dependence is made clear in the plot of the fitted H_{c1} magnitudes in Figs. 4(c) and 4(d). Comparing the data for the two samples, it is clear that this low-temperature increase is far greater in the pristine sample, where the magnitudes of the H_{c1} peaks surpass the measured magnitudes at 57 K. However, the substituted sample still displays a marked increase below 30 K in comparison to the values at 48 K.

Once again, this could be due to a shift in the frequency dependence, suppression of phase coexistence, or metastable effects. However, considering frequency dependence, it is unlikely for the χ'' peak height to first reduce and then increase if the characteristic frequency varies monotonically with temperature. Furthermore, one would expect that metastable effects would suppress the peak height more at lower temperatures due to the reduction of available thermal energy. In comparison to MnSi and $Fe_{1-x}Co_xSi$, where there appears to be little-to-no χ'' signal enhancement at low temperatures [34,36,39], the different low-temperature behavior observed here in the χ'' data of Cu_2OSeO_3 is significant and is explored and explained in the context of the SANS data in later sections.

C. Metastable skyrmions

Finally, the features associated with metastable skyrmions in the FC data will be examined. In Figs. 3(b1) and 3(b2), both samples exhibit a drop in χ' at around 20 mT after FC. This is indicative of the formation of metastable skyrmions at 48 and 49 K, as displayed by the yellow hashed regions. The signal is far greater in the substituted sample, suggesting that the volume of metastable skyrmions which survived the cooling process was far greater in comparison to the pristine sample, as observed previously [53]. When considering the extent of this metastable skyrmion phase, we can see that there is a lack of corresponding χ'' signals in Figs. 3(b3) and 3(b4). Following the argument mentioned previously, this can be expected for a first-order phase transition from a metastable state, where the oscillating probe field only drives the transition in one direction.

Nevertheless, we can estimate the skyrmion phase boundary using the χ' data. It is expected that as the skyrmions annihilate at higher fields, the value of χ' in the FC data will increase until it follows the ZFC values, as shown in Figs. 3(b1), 3(b2), 3(c1), and 3(c2), indicating all skyrmions have decayed to the conical state. We use this assumption to estimate the H_{s2} point for both samples at all temperatures, as summarized by the filled yellow region in Figs. 4(a) and 4(b).

For decreasing field, determining the value of H_{s1} using the χ' data is more complicated. If the skyrmions decay into the conical state before the helical state becomes energetically favored at the H_{c1} point, then we can expect the FC data to follow the HFC data to 0 mT. This is the scenario observed at higher temperatures in both samples, for example, in Figs. 3(b1) and 3(b2), suggesting that metastable skyrmions are annihilated before, or at, the helical-conical boundary.

At lower temperatures, the FC data in the pristine sample follows the HFC data below 20 mT, suggesting that few, or possibly no, metastable skyrmions survived the cooling process down to 10 K. A previous work looking at a pristine Cu_2OSeO_3 sample also noted a lack of metastable skyrmions surviving in this region of the phase diagram with the field applied parallel to [110] [33]. In contrast, for the substituted sample, below 20 mT the FC data follows closer to the ZFC data, as seen in Figs. 3(c1) and 3(c2). This suggests that Zn substitution prevents the metastable skyrmions from decaying into the helical state during the FC process. Future SANS studies will be useful to clarify this behavior.

Examination of the FC χ'' data at 10 K in Figs. 3(c3) and 3(c4) further supports this interpretation. In the substituted sample, at 30 K and below, two additional small peaks are exhibited. Since they appear only in the FC data and only in the substituted sample, it is reasonable to assume that these are associated with the presence of metastable skyrmions. The first feature, labeled H_{s1}^a, appears just below the cooling field of 20 mT. The second feature, labeled H_{s1}^b, is a small peak just below 0 mT. We have distinguished this possible low-field skyrmion region, S*, by the second filled yellow area in Figs. 3(c4) and 4(d). However, we argued previously that the annihilation of metastable skyrmions should exhibit no χ'' signal due to the lack of dissipation in metastable phase transitions. Therefore further study is required to fully understand the origin of these dynamic features and whether they are truly associated with the presence of metastable skyrmions.

VI. SMALL-ANGLE NEUTRON SCATTERING

While the AC susceptibility measurements provide useful information, their interpretation is only able to provide an indication of the details of the underlying associated phenomena. However, SANS measurements provide a more detailed picture of the microscopic behavior, allowing the relative volumes and behavior of each magnetic structure to be compared and contrasted when following each measurement procedure. We performed SANS measurements at both ∼50 K (Figs. 5–7) and 5 K (Figs. 8–10), with the samples in both the field-parallel and field-perpendicular configurations. At both temperatures and for both samples, the intensity of the H1, H2,3, C, and S magnetic peaks are plotted as a function of applied magnetic field in Figs. 5 and 8. These intensities were determined by summing the scattering in the sector boxes defined in Figs. 1(d)–1(k) at each field point. The vertical lines in each figure show the critical fields determined by AC susceptibility measurements at the same temperatures following the ZFC, HFC, and FC procedures.

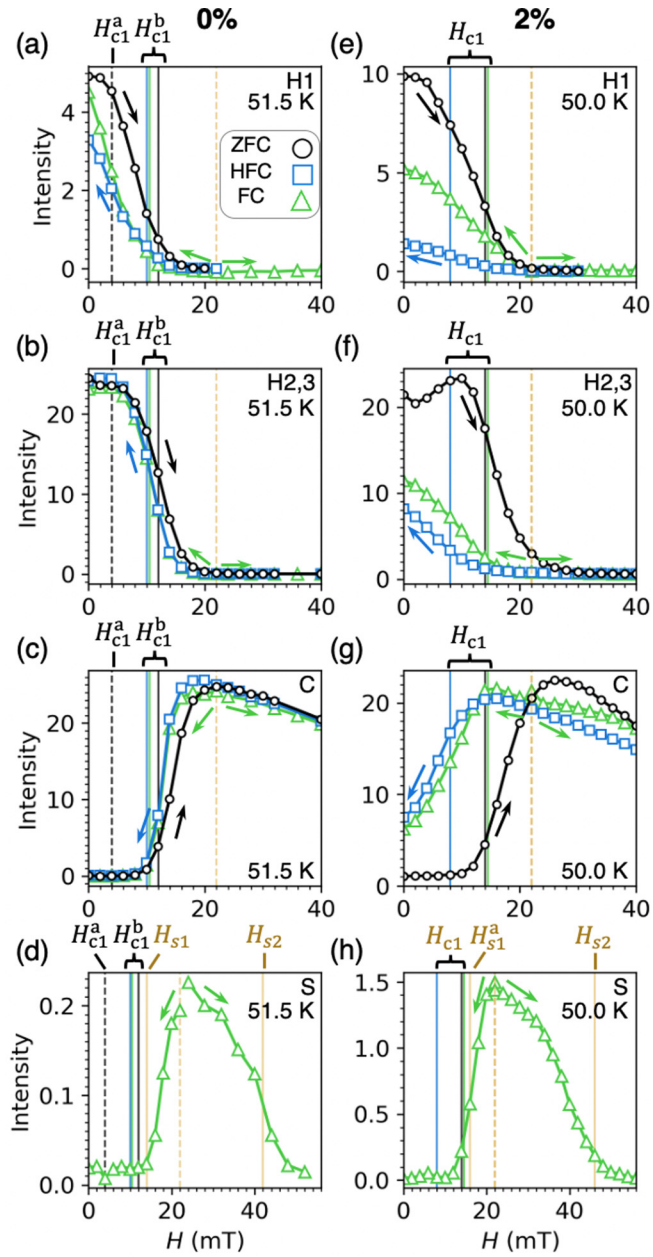

FIG. 5. The neutron-scattering intensity of the H1, H2,3, C, and S peaks measured in the pristine sample at 51.5 K (a–d) and the substituted sample at 50.0 K (e–h) as a function of applied magnetic field for the ZFC (black circles), HFC (blue squares), and FC (green triangles) measurement procedures. The intensities shown were determined by summing the total counts in the sector boxes as defined in Fig. 1. Vertical lines indicate critical fields determined by AC susceptibility measurements. Error bars are too small to be seen.

Representative SANS patterns for these field scans are displayed in the upper panels of each subplot in Figs. 6, 7, 9, and 10. For each scattering pattern, the intensity over a q range of 0.07 and 0.13 nm^{-1} was summed radially at each azimuthal angle ϕ around the center of diffraction, as illustrated in Fig. 1(g). By reducing the dimensionality of the data in this way, the behavior and evolution of the magnetic scattering peaks at each temperature can be examined as a function of the applied magnetic field in a single color plot, as shown in the bottom panel of each subplot in Figs. 6 and 7 (∼50 K), and Figs. 9 and 10 (5 K). In the following sections we shall examine and interpret this SANS data while making reference to the features of the corresponding AC susceptibility data in Figs. 3 and 4.

A. High-temperature SANS

We first consider the SANS data measured at ∼ 50 K. The intensity of H1 in the pristine sample, plotted in Fig. 5(a), exhibits a different low-field behavior for the ZFC and HFC measurements. This can be seen clearly in the SANS patterns in Figs. 6(a) and 6(b), where the intensity of the H1 magnetic satellites at 0 mT is comparatively lower after HFC. This effect is enhanced in the substituted sample, showing an even greater difference between the ZFC and HFC measurements in Fig. 5(e), as illustrated by the SANS data in Figs. 6(d) and 6(e). This suggests that during the transition from the conical state to the helical state with decreasing magnetic field, the H1 helical domains are formed at a lower volume fraction, with the Zn substitution accentuating this effect. This fits with the observations gleaned from the χ' data at around 0 mT in Fig. 3(b), where the HFC value is greater compared to the ZFC value, which hinted at altered helical domain populations. This phenomena might be expected when considering the orientation of the conical and helical domains in Figs. 1(c) and 1(f): the conical domains must rotate by 45 degrees to reorient to the H2,3 helical domains, which might require less energy than the 90-degree rotation required to reorient to the H1 helical domain, and it appears that pinning in the substituted sample accentuates this effect.

In both Figs. 5(d) and 5(h) the skyrmion scattering intensity for each sample is displayed, exhibiting the broad range of field over which metastable skyrmions exist. The H_{s1} and H_{s2} values estimated from the features seen in the χ'' data in Fig. 3 align well with the field extent of the skyrmion scattering in both Figs. 5(d) and 5(h), and illustrate that, at this temperature, the metastable skyrmions decay before the conical-helical phase boundary. The skyrmion peaks can be seen clearly in Figs. 6(c) and 6(f). The greater relative intensity of the S satellites in the substituted sample confirms the formation of a larger population of metastable skyrmions, as was indicated by the AC susceptibility measurements.

In both samples the H1 intensity at 0 mT is higher after FC in comparison to HFC. Given that the primary difference between these two measurement procedures is the formation and subsequent annihilation of metastable skyrmions, this suggests that the skyrmion state preferentially annihilates to H1 helical domains upon decreasing magnetic fields. This finding fits with the previously proposed skyrmion lattice-to-helical-state decay process, whereby skyrmion tubes are zipped together through the motion of Bloch points [26], forming helical domains. In this process formation of H1 domains would likely be preferred over the H2,3 domains, because they modulate in the same plane as the skyrmion lattice, as can be seen by comparing Figs. 1(c) and 1(f).

The intensities of H2,3 and C for the pristine sample, plotted in Figs. 5(b) and 5(c), shows only minor differences between the three procedures, with a slight field offset in the

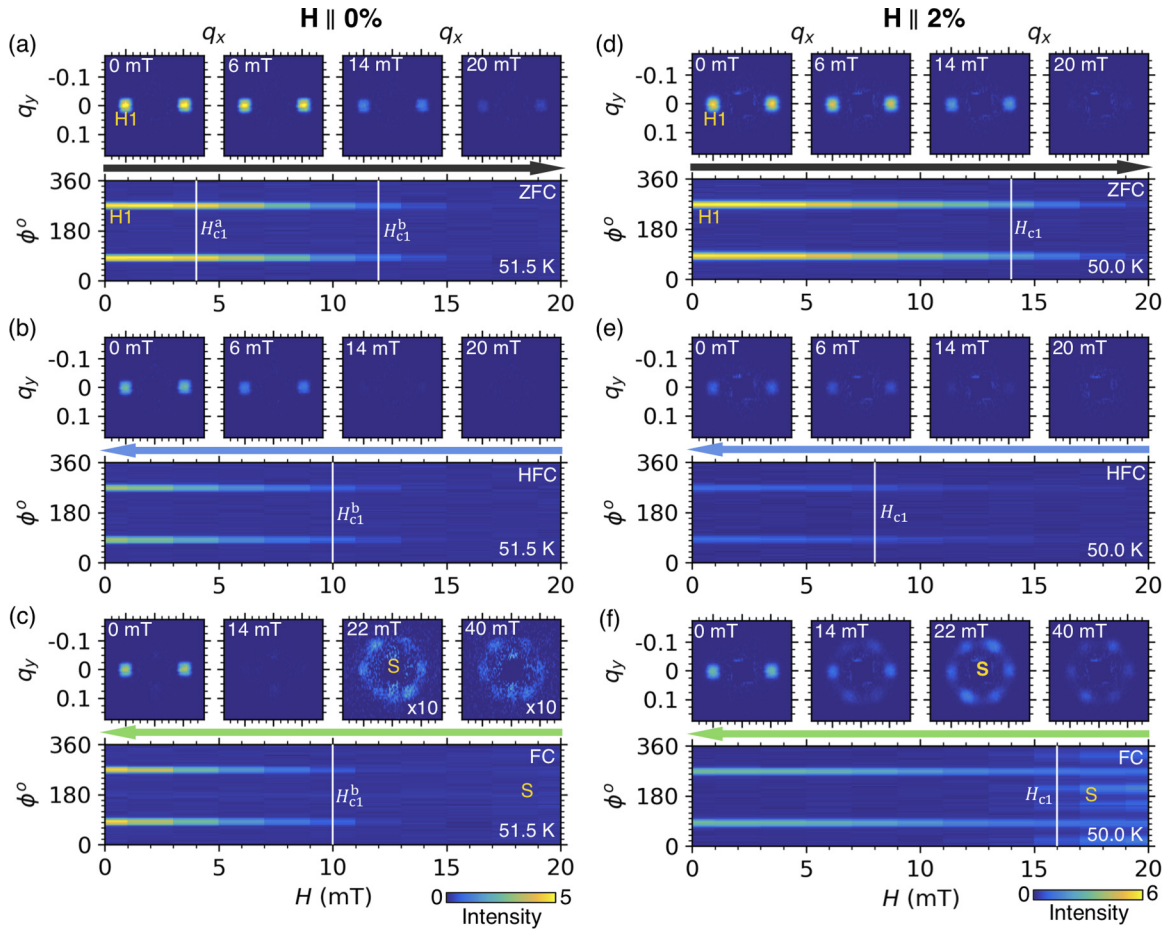

FIG. 6. SANS patterns measured following the ZFC, HFC, and FC procedures in the field-parallel configuration with the pristine sample at 51.5 K (a–c) and the substituted sample at 50.0 K (d–f). The upper panels display SANS patterns at selected fields, while the lower panels display the radially integrated intensity as a function of field and azimuthal angle, ϕ, around the ring of scattering. Vertical lines indicate critical fields determined by AC susceptibility measurements. The units of $q_{x,y}$ are nm^{-1}. For the data presented in each sample configuration, the color scale has been fixed to enable direct comparison between images.

observed behavior. The SANS patterns for the ZFC procedure in Fig. 7(a) demonstrate that, at this temperature, the helical satellites rotate to their position in the conical state as a function of applied magnetic field. This indicates that the propagation vectors of the H2 and H3 helical domains themselves continuously rotate during the phase transition, maintaining long-range magnetic order throughout, with no coexistence of helical and conical states. This behavior is replicated for the reverse conical-to-helical phase transition, as shown in Figs. 7(b) and 7(c). These processes, occurring as a continuous rotation of the magnetic structure, appear more like a second-order rather than first-order phase transition, presumably due to some metastable pinning effects. The observed suppression of helical and conical phase coexistence provides an explanation of the reduction of the H_{c1} χ'' peak at these temperatures in the AC susceptibility data in Fig. 4, as argued in Sec. IV.

On the other hand, in the substituted sample the intensity of the H2,3 peaks and C peaks, plotted in Figs. 5(f) and 5(g), show significant differences between the ZFC, HFC, and FC measurements. The ZFC SANS patterns in Fig. 5(d) depict a gradual rotation of the helical domains to the conical state, similar to that of the pristine sample but occurring at a higher applied magnetic field. However, at 0 mT in the HFC and FC measurements, in Figs. 5(e) and 5(f) we see that the rotation of the conical state back to the helical state is incomplete: the magnetic structures remain partially pinned along the applied field direction. This behavior strongly agrees with that seen in the AC susceptibility data at these temperatures in Fig. 3(b): the substituted sample displayed a larger discrepancy in the value of χ' between the ZFC and HFC data at around 0 mT, which hinted at an altered helical state after HFC. The AC data also showed an even greater suppression of the χ'' signal at H_{s1}, and this is explained by the observed metastable effects in the HFC SANS data. In comparison to the pristine sample, this hysteretic behavior indicates that the presence of Zn in the substituted sample introduces a pinning effect which hinders the reorientation of the helical and conical states.

B. Low-temperature SANS

We turn now to the SANS measurements performed at 5 K, shown in Figs. 8, 9, and 10. Looking at the ZFC data for the pristine sample in Fig. 8(a), the H1 peak gradually decreases in intensity at higher fields. Simultaneously, the intensity of

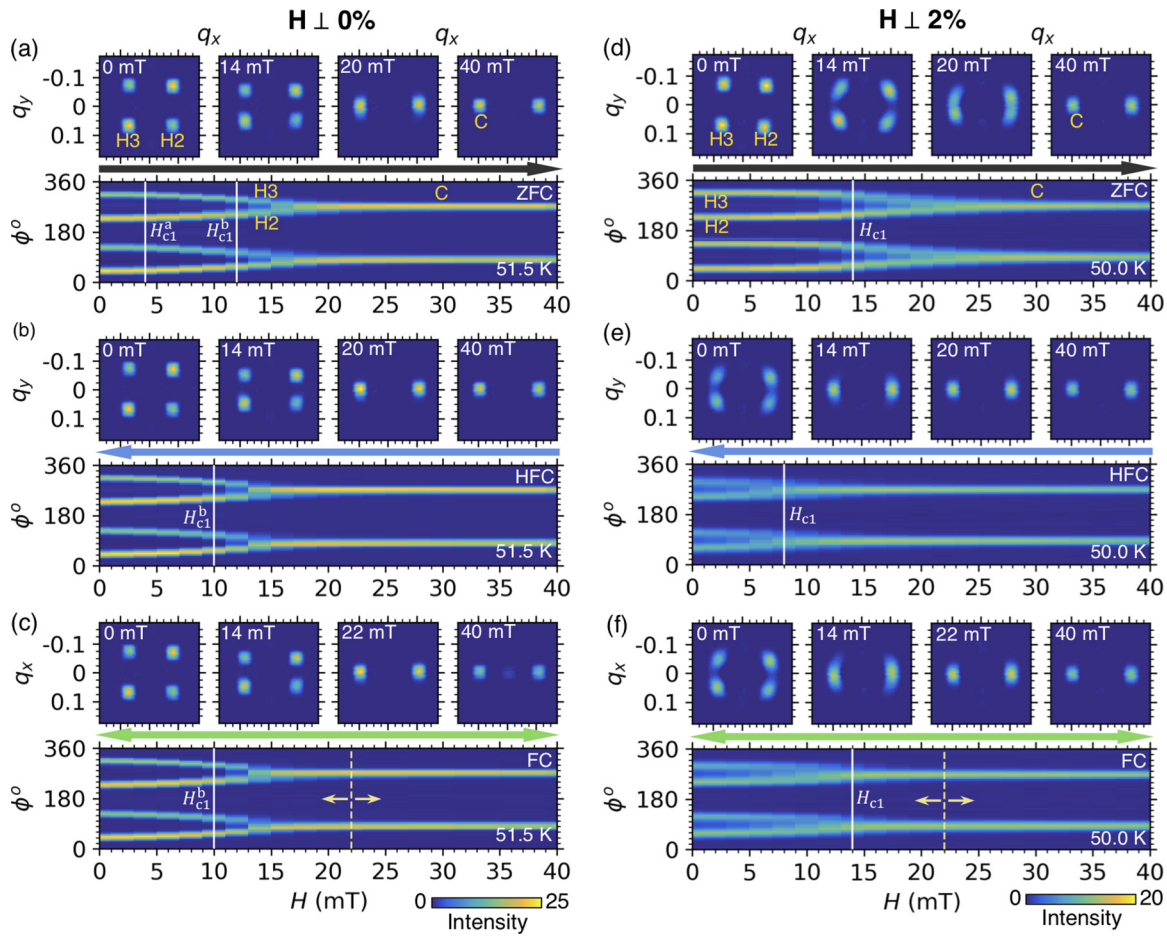

FIG. 7. SANS patterns measured following the ZFC, HFC, and FC procedures in the field-perpendicular configuration with the pristine sample at 51.5 K (a–c) and the substituted sample at 50.0 K (d–f). The upper panels display SANS patterns at selected fields, while the lower panels display the radially integrated intensity as a function of field and azimuthal angle, ϕ, around the ring of scattering. Solid vertical lines indicate critical fields determined by AC susceptibility measurements. Dashed vertical lines and arrows indicate the starting field of the FC measurements. The units of $q_{x,y}$ are nm^{-1}. For the data presented in each sample configuration, the color scale has been fixed to enable direct comparison between images.

the H2,3 peaks initially increases before decreasing after the critical field of H^b_{c1}, where the conical state becomes favored, as shown in Fig. 8(b). In contrast, in the ZFC data of the substituted sample, shown in Figs. 8(d) and 8(e), the H1 and H2,3 peak intensities are almost constant until just before H_{c1} at $\sim$ 30 mT. Here H1 begins to decrease, while the H2,3 intensity shows a small increase when approaching H_{c1} and then decreases.

This could indicate that in the pristine sample the population of H1 helical domains steadily transforms to H2,3 helical domains as a function of field, as the degeneracy of the helical domains is lifted under an increasing applied magnetic field, and the H2,3 helical domains are energetically favored before H^b_{c1}. On the other hand, in the substituted sample this processes is largely suppressed. The observed behavior may explain the presence of the additional H^a_{c1} χ'' peaks observed during ZFC in the pristine sample in Fig. 3 but not in the substituted sample. Another explanation of this behavior could be a distortion of the helical state with increasing field [66], which would explain the drop in H1 intensity but not the increase in H2,3 intensity.

Turning now to the HFC measurements for the pristine sample, in comparison to the 51.5-K data, we see an further reduction in the H1 intensity at 0 mT relative to the ZFC data, as seen in Figs. 8(a) and 9(b). Considering Figs. 8(d) and 9(d), we can see that the difference in HFC behavior between the pristine and substituted samples is less pronounced than it was at $\sim$50 K. This suggests that at lower temperatures, the reduction in H1 domain population after HFC is largely due to energetic considerations, and pinning from the chemical substitution has less effect.

The intensities of the H2,3 helical domain peaks measured in both the pristine and substituted samples are shown in Figs. 8(b) and 8(e). Looking at both the H2,3 and C peak intensities, there is a dramatic field offset in the observed trends for the substituted sample, agreeing with the significant hysteresis displayed by the χ'' peak position in the AC data relative to the pristine sample in Fig. 3. In the pristine sample the H2,3 intensity at 0 mT is higher after HFC than in the ZFC process, again suggesting that H2,3 helical domains are favored when the conical state transforms to the helical state with decreasing field.

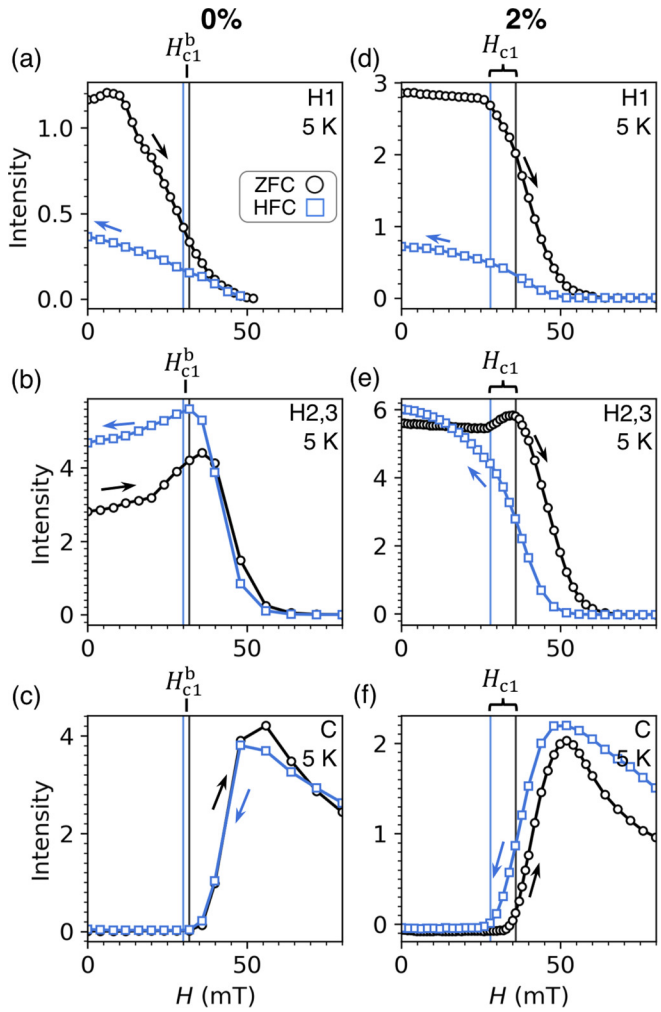

FIG. 8. The neutron-scattering intensity of the H1, H2,3, and C peaks measured in the pristine sample (a–c) and the substituted sample (d–f) at 5 K as a function of applied magnetic field for the ZFC (black circles) and HFC (blue squares) measurement procedures. The intensities shown were determined by summing the total counts in the sector boxes as defined in 1. Vertical lines indicate critical fields determined by AC susceptibility measurements. Error bars are too small to be seen.

In the 50-K measurements of the substituted sample, the H2,3 satellites showed a large reduction in intensity at 0 mT for the HFC measurements, caused by pinning of the magnetic domains as they rotated from the conical to the helical state. However, notably, at this lower temperature, H2,3 intensity is higher at 0 mT after HFC in comparison to the ZFC data, exhibiting similar low-temperature behavior to the pristine sample. This is surprising, as one might expect the effects of pinning to be greater at lower temperatures.

Figure 10 reveals the details of the altered low-temperature behavior. In Figs. 10(a) and 10(b) we see the helical-to-conical phase transition in the field-perpendicular configuration. At 51.5 K, the phase transition was characterized by a continuous rotation of the magnetic structures as a function of applied field, and phase coexistence was suppressed. In contrast, at 5 K the simultaneous detection of both helical and conical peaks in one SANS pattern indicates phase coexistence, as expected for a first-order phase transition.

The altered low-temperature behavior is more clearly evident in the 2% sample, as shown in Figs. 10(c) and 10(d). After HFC at 50 K, the Zn substitution hindered the continuous rotation of the conical structure to the helical state. However, at 5 K we see that at 0 mT the helical domains fully reorient to the [100] and [010] directions after HFC. As in the pristine sample, there is phase coexistence of the helical and conical states for both ZFC and HFC processes. This implies that the pinning which hindered the domain reorientation at higher temperature does not affect the phase transition in the same manner at low temperature.

VII. THE ROLE OF CUBIC ANISOTROPY

To investigate and understand this behavior further, we performed a set of temperature-dependent SANS measurements on the substituted sample in the field-perpendicular orientation. For the first measurement, the sample was HFC at 200 mT to 50 K and then the magnetic field was decreased to 0 mT, forming the pinned helical state, as seen previously in Fig. 7(e). From this point SANS measurements were performed as the sample was cooled to 5 K, and, after resetting the magnetic state upon a subsequent cooling procedure, as the sample was heated from 50 to 58 K. The resulting SANS data is shown in Fig. 11(a). For increasing temperature data, the partially pinned helical state gradually rotates and orients along the ⟨100⟩ axes at higher temperatures before disappearing at T_C. This can be expected, as at higher temperatures there is more energy available to overcome the pinning energy. However, we can see that upon decreasing the temperature from 50 to 5 K, the helices start to reorient to the ⟨100⟩ axes below 40 K, despite the reduction in available thermal energy. This suggests that another contribution must be providing the energy to overcome the pinning at low temperatures.

In these skyrmion-hosting helimagnets, the orientation of the helical domains is determined by the cubic anisotropy. As discussed in the Introduction, recent studies have shown that the anisotropy constant in Cu_2OSeO_3 greatly increases in magnitude below 40 K [29]. This provides an explanation for the observed behavior in this study: the cubic anisotropy becomes strong enough at low temperature to overcome the pinning of the conical-helical reorientation in both the pristine and substituted sample. Due to the interest in the skyrmion phase at high temperatures close to T_C, there have not been many AC susceptibility and SANS measurements reported at low temperatures in these materials. However, from the previously reported AC susceptibility measurements we have surveyed and referenced investigating MnSi and $Fe_{1-x}Co_xSi$ [34,36,39], it appears that the larger low-temperature χ'' signal at the helical-conical phase boundary may be unique to Cu_2OSeO_3. This suggests that the cubic anisotropy term could be responsible for the difference in helical and conical phase coexistence at low and high temperatures in our data.

There are other noticeable effects of the increased cubic anisotropy strength in Cu_2OSeO_3. In the archetypal skyrmion material MnSi, it has been observed that the H_{c1} value does not change dramatically as a function of temperature [39]. Since the value of H_{c1} in an indicator of the strength of the

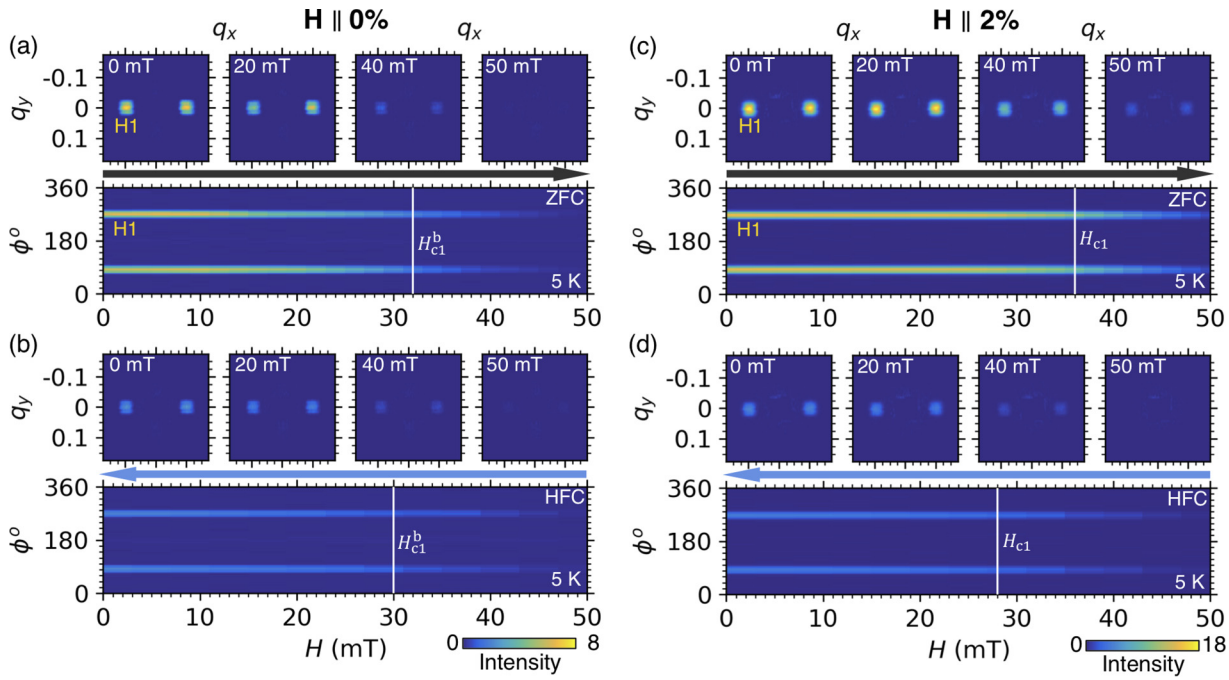

FIG. 9. SANS patterns measured following the ZFC and HFC procedures in the field-parallel configuration with the pristine sample (a, b) and the substituted sample (c, d) at 5 K. The upper panels display SANS patterns at selected fields, while the lower panels display the radially integrated intensity as a function of field and azimuthal angle, ϕ, around the ring of scattering. Vertical lines indicate critical fields determined by AC susceptibility measurements. The units of $q_{x,y}$ are nm^{-1}. For the data presented in each sample configuration, the color scale has been fixed to enable direct comparison between images.

cubic anisotropy, this illustrates that the anisotropy does not significantly change as a function of temperature. In comparable chemically doped materials such as $Fe_{1-x}Co_xSi$ and $Mn_{1-x}Fe_xSi$, the measured value of H_{c1} greatly increases with decreasing temperature; however this is suggested to be due to the pinning of the helical-conical phase transition

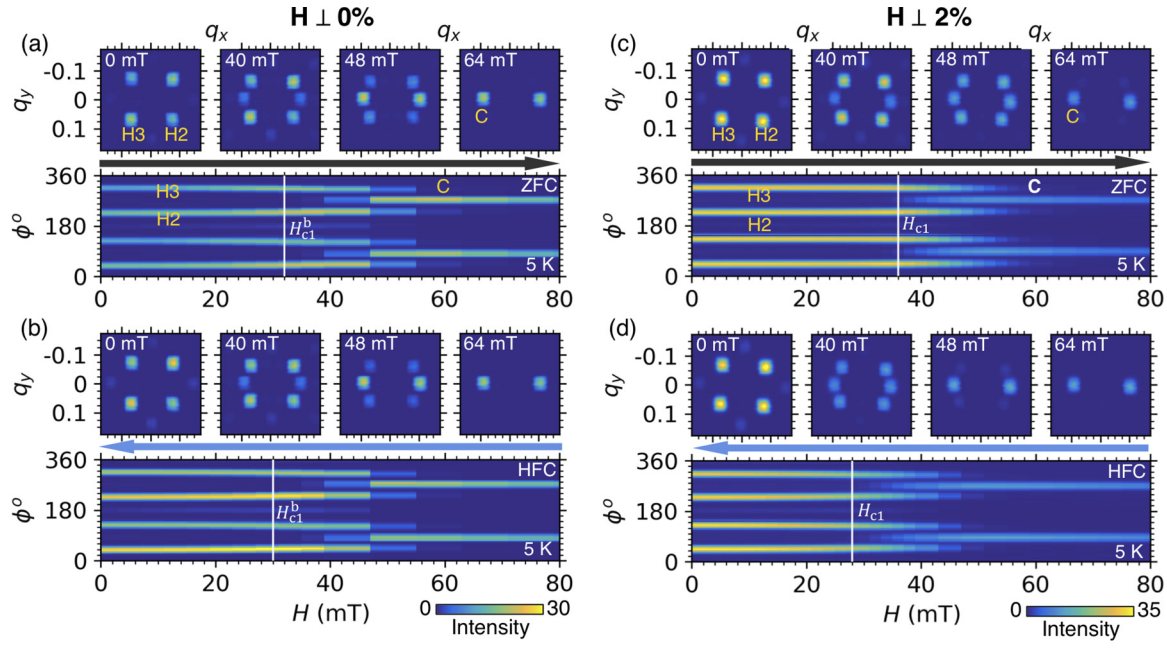

FIG. 10. SANS patterns measured following the ZFC and HFC procedures in the field-perpendicular configuration with the pristine sample (a, b) and the substituted sample (c, d) at 5 K. The upper panels display SANS patterns at selected fields, while the lower panels display the radially integrated intensity as a function of field and azimuthal angle, ϕ, around the ring of scattering. Vertical lines indicate critical fields determined by AC susceptibility measurements. The units of $q_{x,y}$ are nm^{-1}. For the data presented in each sample configuration, the color scale has been fixed to enable direct comparison between images.

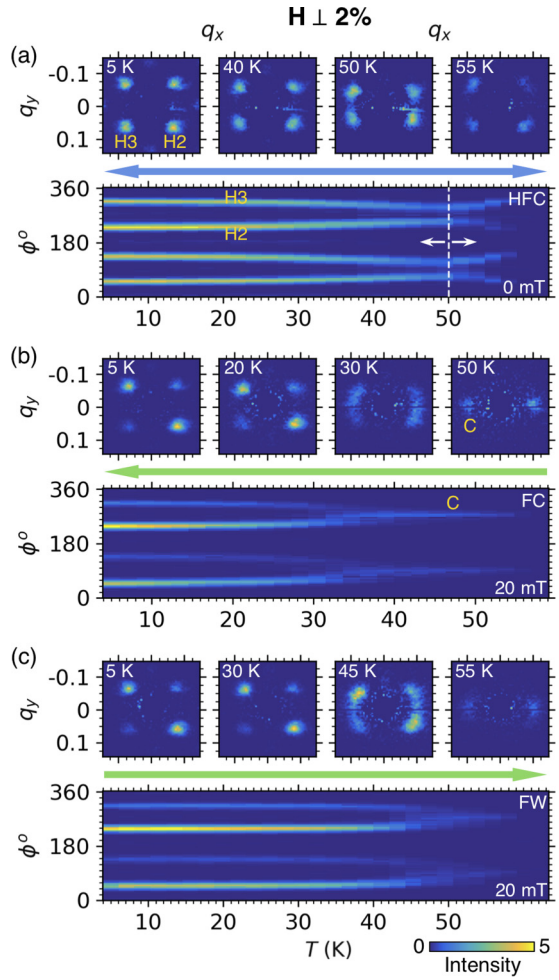

FIG. 11. SANS data measured as a function of temperature after high-field cooling (HFC) to 0 mT (a), while field cooling (FC) to 5 K (b), and field warming to 58 K (c). The upper panels display SANS patterns at selected temperatures, while the lower panels display the radially integrated intensity as a function of temperature and azimuthal angle, ϕ, around the ring of scattering. The units of $q_{x,y}$ are nm^{-1}.

[11,35,36,39]. This is concluded by noting that, upon decreasing the field from the conical state, such as after HFC or FC, the pinning effects are strong enough to fully prevent reorientation to the helical state, even close to T_C [34]. This is similar to the behavior we saw at 50 K in the Zn-substituted sample in this study.

In contrast, the behavior of H_{c1} as a function of temperature in both the pristine and substituted Cu_2OSeO_3 samples in this study are remarkably similar. This is highlighted in Figs. 4(a) and 4(b): both samples display an increase in H_{c1} at lower temperatures. Although the substituted sample does exhibit an offset in H_{c1} between ZFC and HFC measurements, these are small compared to the effect seen in other chemically substituted materials. This limited history-dependent behavior in both samples indicates that the dominant determinant of H_{c1} value in Cu_2OSeO_3 is the strong, temperature-dependent cubic anisotropy, which at low temperature is able to largely overcome the effects of pinning introduced by the nonmagnetic Zn dopant.

A final consideration in the context of the role of cubic anisotropy is the behavior of metastable skyrmions. In previous studies, when FC through the skyrmion pocket in the materials such as MnSi, $Fe_{1-x}Co_xSi$, and $Mn_{1-x}Fe_xSi$, the skyrmion state coexists with the conical state down to base temperature and the helical state is not observed [34,36]. On the other hand, in Cu_2OSeO_3, due to the increase of H_{c1} at low temperatures, the helical phase manifests below 35 K when FC the sample at 20 mT, as seen by the transition of the C to H2,3 magnetic satellites in Fig. 11(b). A similar transition is seen upon field warming (FW) in Fig. 11(c) but at a higher temperature. As speculated, when considering the FC χ' data in Fig. 3, it is likely that the emergence of the helical state while FC results in the loss of the metastable skyrmion population. Such losses might be limited by avoiding the helical phase during the FC process: by cooling at 20 mT to 40 K, increasing the field to 40 mT, and then continuing the cooling process.

VIII. CONCLUSIONS

A combination of detailed AC susceptibility magnetometry and small-angle neutron scattering was utilized to study the phase transitions between, and relative volumes of, the helical, conical, and skyrmion states in both pristine and Zn-substituted Cu_2OSeO_3. Comparison of the data between the samples, and three distinct measurement protocols, resulted in a number of observations and conclusions.

Measurements in both samples have demonstrated that upon HFC, the H1 helical domain volume fraction at 0 mT is reduced after HFC in comparison to ZFC at both high and low temperature, with the effect greater in the Zn-substituted sample. This can be understood when considering the 90-degree rotation required to transform the conical state to the H1 helical orientation, which likely imposes a larger energy barrier in comparison to the 45-degree rotation required to form the H2,3 helical domains. In contrast, the larger H1 intensity at 0 mT after the FC protocol indicates that the metastable skyrmion state preferentially decays to H1 helical domains, lending support to the previously proposed skyrmion-to-helical decay mechanism: the zipping together of skyrmion tubes via the motion of magnetic Bloch points.

In the pristine sample, an additional low-field peak in the ZFC χ'' data suggested a further phase transition, which was identified to be H1 helical domains transforming to H2,3 domains as the helical domain degeneracy is lifted by the applied field before the helical-to-conical phase boundary at H_{c1}. The lack of this peak in the substituted sample suggests that this reorientation is effectively prevented by the introduction of pinning.

At 51.5 K, the pristine sample SANS data revealed that the helical-conical phase transition, for both ZFC and HFC procedures, is characterized by a continuous rotation of the H2,3 helical domains towards the conical state as a function of the applied field and suppression of phase coexistence. This was accompanied by a dramatic reduction in the corresponding χ'' dissipation peak, indicative of suppression of phase coexistence in a first-order phase transition. In the substituted sample at 50.0 K, the magnetic texture did not fully reorient to the ⟨100⟩ helical domain axes upon decreasing field to 0 mT

after HFC, suggesting they were partially pinned along the magnetic field direction. This behavior appears to be consistent with that seen in other substituted helimagnets, where the disorder introduces a similar pinning effect.

In contrast, at 5 K the SANS data illustrated that the same phase transition displayed a coexistence of the helical and conical phases. The corresponding peaks in the χ'' data greatly increase in magnitude at lower temperature, as expected for a first-order transition exhibiting phase coexistence. Remarkably, the pinning effects which dominated the magnetic reorientations in the substituted sample at 50 K appear to be overcome at this lower temperature, despite the reduction of available thermal energy. In comparison to other archetypal helimagnets, this behavior appears to be unique to Cu_2OSeO_3. We attribute this low-temperature behavior to the large, temperature-dependent cubic anisotropy energy present in Cu_2OSeO_3: at low temperature, the anisotropy becomes strong enough to overcome the pinning energy in the absence of thermal activation. The relatively moderate history dependence of the helical-conical phase boundary in both the pristine and substituted samples demonstrates the dominance of this aniosotropic energy contribution.

Overall, these results highlight further unique behavior exhibited by the magnetic phase transitions in Cu_2OSeO_3 due to its comparatively large, temperature-dependent cubic anisotropy. Comparisons between pristine and substituted samples reveal the role of disorder in the slowing down and pinning of the helimagnetic phase transition dynamics, highlighting that these may be effectively overcome by other energy contributions. Consideration and further study of these effects will be crucial when utilizing chemical substitution, or doping, to manipulate the delicate energy balance for exploitation in future applications of skyrmion materials.

ACKNOWLEDGMENTS

This work was supported by the UK Skyrmion Project EPSRC Programme Grant (No. EP/N032128/1). Experiments at the ILL neutron source were supported by experiment time awarded under Proposal No. 5-42-488. Experiments at the ISIS Pulsed Neutron and Muon Source were supported by a beamtime allocation from the Science and Technology Facilities Council, Proposal No. 1920655. M.N.W. acknowledges the support of the Natural Sciences and Engineering Research Council of Canada (NSERC).

[1] U. K. Röß ler, A. N. Bogdanov, and C. Pfleiderer, Spontaneous skyrmion ground states in magnetic metals, Nature (London) **442**, 797 (2006).

[2] J. Iwasaki, M. Mochizuki, and N. Nagaosa, Current-induced skyrmion dynamics in constricted geometries, Nat. Nanotechnol. **8**, 742 (2013).

[3] N. Nagaosa and Y. Tokura, Topological properties and dynamics of magnetic skyrmions, Nat. Nanotechnol. **8**, 899 (2013).

[4] I. Dzyaloshinskii, A thermodynamic theory of "weak" ferromagnetizm of antiferromagnetics, J. Phys. Chem. Solids **4**, 241 (1958).

[5] S. Heinze, K. von Bergmann, M. Menzel, J. Brede, K. Kubetzka, R. Wiesendanger, G. Bihlmayer, and S. Blügel, Spontaneous atomic-scale magnetic skyrmion lattice in two dimensions, Nat. Phys. **7**, 713 (2011).

[6] A. Fert, V. Cros, and J. Sampaio, Skyrmions on the track, Nat. Nanotechnol. **8**, 152 (2013).

[7] S. Woo, K. Litzius, B. Krüger, M.-Y. Im, L. Caretta, K. Richter, M. Mann, A. Krone, R. M. Reeve, M. Weigand, P. Agrawal, I. Lemesh, M.-A. Mawass, P. Fischer, M. Kläui, and G. S. D. Beach, Observation of room-temperature magnetic skyrmions and their current-driven dynamics in ultrathin metallic ferromagnets, Nat. Mater. **15**, 501 (2016).

[8] S. Mühlbauer, B. Binz, F. Jonietz, C. Pfleiderer, A. Rosch, A. Neubauer, R. Georgii, and P. Böni, Skyrmion lattice in a chiral magnet, Science **323**, 915 (2009).

[9] A. Neubauer, C. Pfleiderer, B. Binz, A. Rosch, R. Ritz, P. G. Niklowitz, and P. Böni, Topological Hall Effect in the A Phase of MnSi, Phys. Rev. Lett **102**, 186602 (2009).

[10] T. Tanigaki, K. Shibata, N. Kanazawa, X. Yu, Y. Onose, H. S. Park, D. Shindo, and Y. Tokura, Real-space observation of short-period cubic lattice of skyrmions in MnGe, Nano Lett. **15**, 5438 (2015).

[11] W. Münzer, A. Neubauer, T. Adams, S. Mühlbauer, C. Franz, F. Jonietz, R. Georgii, P. Böni, B. Pedersen, M. Schmidt, A. Rosch, and C. Pfleiderer, Skyrmion lattice in the doped semiconductor $Fe_{1-x}Co_xSi$, Phys. Rev. B **81**, 041203(R) (2010).

[12] X. Z. Yu, Y. Onose, N. Kanazawa, J. H. Park, J. H. Han, Y. Matsui, N. Nagaosa, and Y. Tokura, Real-space observation of a two-dimensional skyrmion crystal, Nature (London) **465**, 901 (2010).

[13] H. Wilhelm, M. Baenitz, M. Schmidt, U. K. Rößler, A. A. Leonov, and A. N. Bogdanov, Precursor Phenomena at the Magnetic Ordering of the Cubic Helimagnet FeGe, Phys. Rev. Lett. **107**, 127203 (2011).

[14] X. Z. Yu, N. Kanazawa, Y. Onose, K. Kimoto, W. Z. Zhang, S. Ishiwata, Y. Matsui, and Y. Tokura, Near room-temperature formation of a skyrmion crystal in thin-films of the helimagnet FeGe, Nat. Mater. **10**, 106 (2011).

[15] S. Seki, X. Z. Yu, S. Ishiwata, and Y. Tokura, Observation of skyrmions in a multiferroic material, Science **336**, 198 (2012).

[16] Y. Tokunaga, X. Z. Yu, J. S. White, H. M. Rønnow, D. Morikawa, Y. Taguchi, and Y. Tokura, A new class of chiral materials hosting magnetic skyrmions beyond room temperature, Nat. Commun. **6**, 7638 (2015).

[17] I. Kézsmárki, S. Bordács, P. Milde, E. Neuber, L. M. Eng, J. S. White, H. M. Rønnow, C. D. Dewhurst, M. Mochizuki, K. Yanai, H. Nakamura, D. Ehlers, V. Tsurkan, and A. Loidl, Néel-type skyrmion lattice with confined orientation in the polar magnetic semiconductor GaV_4S_8, Nat. Mater. **14**, 1116 (2015).

[18] E. Ruff, S. Widmann, P. Lunkenheimer, V. Tsurkan, S. Bordács, I. Kézsmárki, and A. Loidl, Multiferroicity and skyrmions carrying electric polarization in GaV_4S_8, Sci. Adv. **1**, e1500916 (2015).

[19] S. Bordács, A. Butykai, B. G. Szigeti, J. S. White, R. Cubitt, A. O. Leonov, S. Widmann, D. Ehlers, H.-A. Krug von Nidda, V. Tsurkan, A. Loidl, and I. Kézsmárki, Equilibrium skyrmion

lattice ground state in a polar easy-plane magnet, Sci. Rep. **7**, 7584 (2017)

[20] P. Bak and M. H. Jensen, Theory of helical magnetic structures and phase transitions in MnSi and FeGe, J. Phys. C: Solid State Phys. **13**, L881 (1980).

[21] K. Karube, J. S. White, N. Reynolds, J. L. Gavilano, H. Oike, A. Kikkawa, F. Kagawa, Y. Tokunaga, H. M. Rønnow, Y. Tokura, and Y. Taguchi, Robust metastable skyrmions and their triangular-square lattice structural transition in a high-temperature chiral magnet, Nat. Mater. **15**, 1237 (2016).

[22] K. Karube, J. S. White, D. Morikawa, M. Bartkowiak, A. Kikkawa, Y. Tokunaga, T. Arima, H. M. Rønnow, Y. Tokura, and Y. Taguchi, Skyrmion formation in a bulk chiral magnet at zero magnetic field and above room temperature, Phys. Rev. Materials **1**, 074405 (2017).

[23] K. Karube, J. S. White, V. Ukleev, C. D. Dewhurst, R. Cubitt, A. Kikkawa, Y. Tokunaga, H. M. Rønnow, Y. Tokura, and Y. Taguchi, Metastable skyrmion lattices governed by magnetic disorder and anisotropy in β-Mn-type chiral magnets, Phys. Rev. B **102**, 064408 (2020).

[24] H. Oike, A. Kikkawa, N. Kanazawa, Y. Taguchi, M. Kawasaki, Y. Tokura, and F. Kagawa, Interplay between topological and thermodynamic stability in a metastable magnetic skyrmion lattice, Nat. Phys. **12**, 62 (2016).

[25] F. Kagawa, H. Oike, W. Koshibae, A. Kikkawa, Y. Okamura, Y. Taguchi, N. Nagaosa, and Y. Tokura, Current-induced viscoelastic topological unwinding of metastable skyrmion strings, Nat. Commun. **8**, 1332 (2017).

[26] P. Milde, D. Köhler, J. Seidel, L. M. Eng, A. Bauer, A. Chacon, J. Kindervater, S. Mühlbauer, C. Pfleiderer, S. Buhrandt, c. Schütte, and A. Rosch, Unwinding of a skyrmion lattice by magnetic monopoles, Science **340**, 1076 (2013).

[27] Y. Okamura, F. Kagawa, S. Seki, and Y. Tokura, Transition to and from the skyrmion lattice phase by electric fields in a magnetoelectric compound, Nat. Commun. **7**, 12669 (2016).

[28] T. Nakajima, H. Oike, A. Kikkawa, E. P. Gilbert, N. Booth, K. Kakurai, Y. Taguchi, Y. Tokura, F. Kagawa, and T. Arima, Skyrmion lattice structural transition in MnSi, Sci. Adv. **3**, e1602562 (2017).

[29] M. Halder, A. Chacon, A. Bauer, W. Simeth, S. Mühlbauer, H. Berger, L. Heinen, M. Garst, A. Rosch, and C. Pfleiderer, Thermodynamic evidence of a second skyrmion lattice phase and tilted conical phase in Cu_2OSeO_3, Phys. Rev. B **98**, 144429 (2018).

[30] A. Chacon, L. Heinen, M. Halder, A. Bauer, W. Simeth, S. Mühlbauer, H. Berger, M. Garst, A. Rosch, and C. Pfleiderer, Observation of two independent skyrmion phases in a chiral magnetic material, Nat. Phys. **14**, 936 (2018).

[31] L. Ludgren, O. Beckman, V. Attia, S. P. Bhattacheriee, and M. Richardson, Helical spin arrangement in cubic FeGe, Phys. Scr. **1**, 69 (1970).

[32] F. Qian, L. J. Bannenberg, H. Wilhelm, G. Chaboussant, L. M. Debeer-Schmitt, M. P. Schmidt, A. Aqee, T. T. M. Palstra, E. Brück, A. J. E. Lefering, C. Pappas, M. Mostovoy, and A. O. Leonov, New magnetic phase of the chiral skyrmion material Cu_2OSeO_3, Sci. Adv. **4**, eaat7323 (2018).

[33] L. J. Bannenberg, H. Wilhelm, R. Cubitt, A. Labh, M. P. Schmidt, E. Lelièvre-Berna, C. Pappas, M. Mostovoy, and A. O. Leonov, Multiple low-temperature skyrmionic states in a bulk chiral magnet, npj Quantum Mater. **4**, 11 (2019)

[34] A. Bauer, M. Garst, and C. Pfleiderer, History dependence of the magnetic properties of single-crystal $Fe_{1-x}Co_xSi$, Phys. Rev. B **93**, 235144 (2016).

[35] L. J. Bannenberg, K. Kakurai, F. Qian, E. Lelièvre-Berna, C. D. Dewhurst, Y. Onose, Y. Endoh, Y. Tokura, and C. Pappas, Extended skyrmion lattice scattering and long-time memory in the chiral magnet $Fe_{1-x}Co_xSi$, Phys. Rev. B **94**, 104406 (2016).

[36] L. J. Bannenberg, A. J. E. Lefering, K. Kakurai, Y. Onose, Y. Endoh, Y. Tokura, and C. Pappas, Magnetic relaxation phenomena in the chiral magnet $Fe_{1-x}Co_xSi$: An ac susceptibility study, Phys. Rev. B **94**, 134433 (2016).

[37] S. V. Grigoriev, V. A. Dyadkin, E. V. Moskvin, D. Lamago, Th. Wolf, H. Eckerlebe, and S. V. Maleyev, Helical spin structure of $Mn_{1-y}Fe_ySi$ under a magnetic field: Small angle neutron diffraction study, Phys. Rev. B **79**, 144417 (2009).

[38] C. Franz, F. Freimuth, A. Bauer, R. Ritz, C. Schnarr, C. Duvinage, T. Adams, S. Blügel, A. Rosch, Y. Mokrousov, and C. Pfleiderer, Real-Space and Reciprocal-Space Berry Phases in the Hall Effect of $Mn_{1-y}Fe_ySi$, Phys. Rev. Lett. **112**, 186601 (2014).

[39] L. J. Bannenberg, F. Weber, A. J. E. Lefering, T. Wolf, and C. Pappas, Magnetization and ac susceptibility study of the cubic chiral magnet $Mn_{1-y}Fe_ySi$, Phys. Rev. B **98**, 184430 (2018).

[40] L. J. Bannenberg, R. M. Dalgliesh, T. Wolf, F. Weber, and C. Pappas, Evolution of helimagnetic correlations in $Mn_{1-y}Fe_ySi$ with doping: A small-angle neutron scattering study, Phys. Rev. B **98**, 184431 (2018).

[41] S. V. Grigoriev, N. M. Potapova, S.-A. Siegfried, V. A. Dyadkin, E. V. Moskvin, V. Dmitriev, D. Menzel, C. D. Dewhurst, D. Chernyshov, R. A. Sadykov, L. N. Fomicheva, and A. V. Tsvyashchenko, Chiral Properties of Structure and Magnetizm in $Mn_{1-y}Fe_yGe$ Compounds: When the Left and the Right are Fighting, Who Wins? Phys. Rev. Lett. **110**, 207201 (2013).

[42] K. Shibata, X. Z. Yu, T. Hara, D. Morikawa, N. Kanazawa, K. Kimoto, S. Ishiwata, Y. Matsui, and Y. Tokura, Towards control of the size and helicity of skyrmions in helimagnetic alloys by spin-orbit coupling, Nat. Nanotechnol. **8**, 723 (2013).

[43] T. Koretsune, N. Nagaosa, and R. Arita, Control of Dzyaloshinskii-Moriya interaction in $Mn_{1-y}Fe_yGe$: A first-principles study, Sci. Rep. **5**, 13302 (2015).

[44] S. V. Grigoriev, E. V. Altynbaev, S.-A. Siegfried, K. A. Pshenichnyi, D. Honnecker, A. Heinemann, and A. V. Tsvyashchenko, Spin-wave dynamics in Mn-doped FeGe helimagnet: Small-angle neutron scattering study, J. Magn. Magn. Mater. **459**, 159 (2018).

[45] Y. Fujishiro, N. Kanazawa, T. Nakajima, X. Z. Yu, K. Ohishi, Y. Kawamura, K. Kakurai, T. Arima, H. Mitamura, A. Miyake, K. Akiba, M. Tokunaga, A. Matsuo, K. Kindo, T. Koretsune, R. Arita, and Y. Tokura, Topological transitions among skyrmion- and hedgehog-lattice states in cubic chiral magnets, Nat. Commun. **10**, 1059 (2019).

[46] R. Takagi, D. Morikawa, K. Karube, N. Kanazawa, K. Shibata, G. Tatara, Y. Tokunaga, T. Arima, Y. Taguchi, Y. Tokura, and S. Seki, Spin-wave spectroscopy of the Dzyaloshinskii-Moriya interaction in room-temperature chiral magnets hosting skyrmions, Phys. Rev. B **95**, 220406(R) (2017).

[47] K. Karube, K. Shibata, J. S. White, T. Koretsune, X. Z. Yu, Y. Tokunaga, H. M. Rønnow, R. Arita, T. Arima, Y. Tokura, and Y. Taguchi, Controlling the helicity of magnetic skyrmions in

a β-Mn-type high-temperature chiral magnet, Phys. Rev. B **98**, 155120 (2018).

[48] K. J. A. Franke, B. M. Huddart, T. J. Hicken, F. Xiao, S. J. Blundell, F. L. Pratt, M. Crisanti, J. A. T. Barker, S. J. Clark, A. Štefančič, M. C. Hatnean, G. Balakrishnan, and T. Lancaster, Magnetic phases of skyrmion-hosting $GaV_4S_{8-y}Se_y$ ($y = 0, 2, 4, 8$) probed with muon spectroscopy, Phys. Rev. B **98**, 054428 (2018).

[49] T. J. Hicken, S. J. R. Holt, K. J. A. Franke, Z. Hawkhead, A. Štefančič, M. N. Wilson, M. Gomilšek, B. M. Huddart, S. J. Clark, M. R. Lees, F. L. Pratt, S. J. Blundell, G. Balakrishnan, and T. Lancaster, Magnetism and Néel skyrmion dynamics in $GaV_4S_{8-y}Se_y$, Phys. Rev. Research **2**, 032001(R) (2020).

[50] H. C. Wu, K. D. Chandrasekhar, T. Y. Wei, K. J. Hsieh, T. Y. Chen, H. Berger, and H. D. Yang, Physical pressure and chemical expansion effects on the skyrmion phase in Cu_2OSeO_3, J. Phys. D **48**, 475001 (2015).

[51] K. D. Chandrasekhar, H. C. Wu, C. L. Huanga, and H. D. Yang, Effects of Jahn–Teller distortion on the skyrmion stability of $(Cu_{1-x}Ni_x)_2OSeO_3$, J. Mater. Chem. C **4**, 5270 (2016).

[52] A. Štefančič, S. H. Moody, T. J. Hicken, M. T. Birch, G. Balakrishnan, S. A. Barnett, M. Crisanti, J. S. O. Evans, S. J. R. Holt, K. J. A. Franke, P. D. Hatton, B. M. Huddart, M. R. Lees, F. L. Pratt, C. C. Tang, M. N. Wilson, F. Xiao, and T. Lancaster, Origin of skyrmion lattice phase splitting in Zn-substituted Cu_2OSeO_3, Phys. Rev. Materials **2**, 111402(R) (2018).

[53] M. T. Birch, R. Takagi, S. Seki, M. N. Wilson, F. Kagawa, A. Štefančič, G. Balakrishnan, R. Fan, P. Steadman, C. J. Ottley, M. Crisanti, R. Cubitt, T. Lancaster, Y. Tokura, and P. D. Hatton, Increased lifetime of metastable skyrmions by controlled doping, Phys. Rev. B **100**, 014425 (2019).

[54] M. N. Wilson, M. Crisanti, C. Barker, A. Štefančič, J. S. White, M. T. Birch, G. Balakrishnan, R. Cubitt, and P. D. Hatton, Measuring the formation energy barrier of skyrmions in zinc-substituted Cu_2OSeO_3, Phys. Rev. B **99**, 174421 (2019).

[55] A. S. Sukhanov, Praveen Vir, A. S. Cameron, H. C. Wu, N. Martin, S. Mühlbauer, A. Heinemann, H. D. Yang, C. Felser, and D. S. Inosov, Increasing skyrmion stability in Cu_2OSeO_3 by chemical substitution, Phys. Rev. B **100**, 184408 (2019).

[56] M.-G. Han, J. A. Garlow, Y. Kharkov, L. Camacho, R. Rov, J. Sauceda, G. Vats, K. Kisslinger, T. Kato, O. Sushkov, Y. Zhu, C. Ulrich, T. Söhnel, and J. Seidel, Scaling, rotation, and channeling behavior of helical and skyrmion spin textures in thin films of Te-doped Cu_2OSeO_3, Sci. Adv. **6**, eaax2138 (2020).

[57] R. Tomasello, E. Martinez, R. Zivieri, L. Torres, M. Carpentieri, and G. Finocchio, A strategy for the design of skyrmion racetrack memories, Sci. Rep. **4**, 6784 (2015).

[58] X. Zhang, G. P. Zhao, H. Fangohr, J. Ping Liu, W. X. Xia, J. Xia, and F. J. Morvan, Skyrmion-skyrmion and skyrmion-edge repulsions in skyrmion-based racetrack memory, Sci. Rep. **5**, 7643 (2015).

[59] I. L. Fernandes, J. Bouaziz, S. Blügel, and S. Lounis, Universality of defect-skyrmion interaction profiles, Nat. Commun. **9**, 4395 (2018).

[60] K. Fallon, S. Hughes, K. Zeissler, W. Legrand, F. Ajejas, D. Maccariello, S. McFadzean, W. Smith, D. McGrouther, S. Collin, N. Reyren, V. Cros, C. H. Marrows, and S. McVitie, Controlled individual skyrmion nucleation at artificial defects formed by ion irradiation, Small **16**, 1907450 (2020).

[61] M. T. Birch, S. H. Moody, O. Bewley, and D. Alba Venero, Dataset: Time-resolved SANS study of the phase transition dynamics in the skyrmion material Cu_2OSeO_3, STFC ISIS Facility, 2019.

[62] C. V. Topping and S. J. Blundell, A. C. susceptibility as a probe of low-frequency magnetic dynamics, J. Phys.: Condens. Matter **31**, 013001 (2018).

[63] M. Balanda, AC susceptibility studies of phase transitions and magnetic relaxation: conventional, molecular and low-dimensional magnets, Acta Phys. Pol. A **124**, 964 (2013)

[64] F. Qian, H. Wilhelm, A. Aqeel, T. T. M. Palstra, A. J. E. Lefering, E. H. Brück, and C. Pappas, Phase diagram and magnetic relaxation phenomena in Cu_2OSeO_3, Phys. Rev. B **94**, 064418 (2016).

[65] I. Levatić, V. Šurija, H. Berger, and I. Živković, Dissipation processes in the insulating skyrmion compound Cu_2OSeO_3, Phys. Rev. B **90**, 224412 (2014).

[66] Y. A. Izyumov, Modulated, or long-periodic, magnetic structures of crystals, Sov. Phys. Uspekhi **27**, 845 (1984).